



HAL
open science

Multi-scale finite element modelling of solidification structures by a splitting method taking into account the transport of equiaxed grains

Thi-Thuy-My Nguyen, Hervé Combeau, Miha Založnik, Michel Bellet,
Charles-André Gandin

► To cite this version:

Thi-Thuy-My Nguyen, Hervé Combeau, Miha Založnik, Michel Bellet, Charles-André Gandin. Multi-scale finite element modelling of solidification structures by a splitting method taking into account the transport of equiaxed grains. MCWASP XIV: International Conference on Modelling of Casting, Welding and Advanced Solidification Processes, Jun 2015, Awaji island, Hyogo, Japan. pp.012007, 10.1088/1757-899X/84/1/012007 . hal-01254391

HAL Id: hal-01254391

<https://minesparis-psl.hal.science/hal-01254391>

Submitted on 12 Jan 2016

HAL is a multi-disciplinary open access archive for the deposit and dissemination of scientific research documents, whether they are published or not. The documents may come from teaching and research institutions in France or abroad, or from public or private research centers.

L'archive ouverte pluridisciplinaire **HAL**, est destinée au dépôt et à la diffusion de documents scientifiques de niveau recherche, publiés ou non, émanant des établissements d'enseignement et de recherche français ou étrangers, des laboratoires publics ou privés.

Multi-scale finite element modelling of solidification structures by a splitting method taking into account the transport of equiaxed grains

T T M Nguyen¹, H Combeau², M Založnik², M Bellet¹, Ch-A Gandin¹

¹ MINES ParisTech, CEMEF UMR CNRS 7635, 06904 Sophia Antipolis, France

² Université de Lorraine, IJL UMR CNRS 7198, 54011 Nancy, France

E-mail: thi-thuy-my.nguyen@mines-paristech.fr

Abstract. In solidification processes of large industrial castings and ingots, the transport of solid in the liquid has an important effect on the final grain structure and macrosegregation. Modeling is still challenging as complex interactions between heat and mass transfers at microscopic and macroscopic scales are highly coupled. This paper first presents a multi-scale numerical solidification model coupling nucleation, grain growth and solute diffusion at microscopic scales with heat and mass transfer, including transport of liquid and solid phases at macroscopic scales. The resolution consists of a splitting method, which considers the evolution and interaction of quantities during the process with a transport stage and a growth stage. This splitting reduces the nonlinear complexity of the set of considered equations and provides an efficient numerical implementation. It is inspired by the work of Založnik *et al.* [1,2], which used a finite volume method (FVM). The present work develops the solution based on the finite element method (FEM). Numerical results obtained with this model are presented and simulations without and with grain transport are compared to study the impact of solid-phase transport on the solidification process and on the formation of macrosegregation.

1. Introduction

Solidification modelling accounting for melt convection and solid movement has been limited. The first important works were proposed with a volume-averaged model consistently connecting microscopic phenomena to macroscopic transports [3-6]. The transport of the solid structure was based on a population balance written for the equiaxed grains. Similar solidification modeling was later further developed [1,2,7-10]. The numerical resolution algorithm proposed by Založnik and Combeau [1] efficiently dealt with the complexity of the strongly coupled problem by using a splitting method. This splitting method was successfully applied to large industrial castings [11]. It is worth noticing that these models were based on the finite volume method (FVM), while the use of the finite element method (FEM) has been rarely considered for volume-averaged multiphase multiscale modelling of solidification. Besides ongoing advancements with FVM, the present study aims at developing FEM solvers when solid transport is to be considered. In this paper, a numerical FEM solidification model is presented accounting for microscopic phenomena as well as for the motion of solid and liquid. First, the macroscopic conservation equations and the constitutive relations describing interfacial interactions and exchanges are summarized. The resolution method and the numerical implementation for the set of non-linear equations are then detailed. Finally, numerical simulations using the current



model are performed to validate the numerical implementation. Results demonstrate an efficient FEM resolution scheme implemented for the purely convective transport problem, which is difficult to solve numerically with the FEM in the absence of diffusive effects.

2. Model description

2.1. Macroscopic conservation equations and constitutive relations

The macroscopic conservation equations of mass, momentum, species and energy for each phase α , (1)-(4) respectively, are obtained by averaging the microscopic equations over a representative elementary volume. Details on this averaging method can be found elsewhere [12].

$$\text{Mass} \quad \frac{\partial(g^\alpha \rho^\alpha)}{\partial t} + \nabla \cdot (g^\alpha \rho^\alpha \langle \mathbf{v}^\alpha \rangle^\alpha) = \Gamma^\alpha + \Phi^\alpha \quad (1)$$

$$\begin{aligned} \text{Momentum} \quad \frac{\partial(g^\alpha \rho^\alpha \langle \mathbf{v}^\alpha \rangle^\alpha)}{\partial t} + \nabla \cdot (g^\alpha \rho^\alpha \langle \mathbf{v}^\alpha \rangle^\alpha \langle \mathbf{v}^\alpha \rangle^\alpha) \\ = -g^\alpha \nabla \langle p \rangle^\alpha + \nabla \cdot (g^\alpha \langle \boldsymbol{\tau} \rangle^\alpha) + g^\alpha \langle \mathbf{f} \rangle^\alpha + \mathbf{M}^{\alpha,d} + \mathbf{M}^{\alpha,\Gamma} + \mathbf{M}^{\alpha,\Phi} \end{aligned} \quad (2)$$

$$\begin{aligned} \text{Species} \quad \frac{\partial(g^\alpha \rho^\alpha \langle w^\alpha \rangle^\alpha)}{\partial t} + \nabla \cdot (g^\alpha \rho^\alpha \langle w^\alpha \rangle^\alpha \langle \mathbf{v}^\alpha \rangle^\alpha) \\ = -\nabla \cdot (g^\alpha \langle \mathbf{j} \rangle^\alpha) + J^{\alpha,J} + J^{\alpha,\Gamma} + J^{\alpha,\Phi} \end{aligned} \quad (3)$$

$$\begin{aligned} \text{Energy} \quad \frac{\partial(g^\alpha \rho^\alpha \langle h^\alpha \rangle^\alpha)}{\partial t} + \nabla \cdot (g^\alpha \rho^\alpha \langle h^\alpha \rangle^\alpha \langle \mathbf{v}^\alpha \rangle^\alpha) \\ = -\nabla \cdot (g^\alpha \langle \mathbf{q} \rangle^\alpha) + Q^{\alpha,J} + Q^{\alpha,\Gamma} + Q^{\alpha,\Phi} \end{aligned} \quad (4)$$

where the superscript α represents phase α ; the notation $\langle \rangle$ indicates the average value; g is the volume fraction; ρ is the mass density; \mathbf{v} is the velocity vector; w is the concentration; h is the enthalpy; p is the pressure; $\boldsymbol{\tau}$ is the viscous stress; \mathbf{f} is the body force per unit volume; \mathbf{j} is the species flux; \mathbf{q} is the heat flux; Γ, Φ are the change rates of mass due to the phase change and the nucleation.

Except Φ , the other terms related to the nucleation, noted with the superscript Φ , are neglected. The change rates of momentum, solute mass and energy due to the phase change are expressed respectively as

$$\mathbf{M}^{\alpha,\Gamma} = \bar{\mathbf{v}}^{\alpha*} \Gamma^\alpha \quad \Bigg| \quad J_i^{\alpha,\Gamma} = \bar{w}^{\alpha*} \Gamma^\alpha \quad \Bigg| \quad Q^{\alpha,\Gamma} = \bar{h}^{\alpha*} \Gamma^\alpha \quad (5)$$

The solute flux at the solid/liquid interface (6) is defined as a function of the difference of the variation between the average solute concentration in the phase $\langle w^\alpha \rangle^\alpha$ and at the interface, $w^{\alpha*}$. Over a representative elementary volume, the temperature is considered to be uniform, therefore the heat flux $Q^{\alpha,J}$ is equal to zero.

$$J^{\alpha,J} = \frac{\rho^\alpha S_V D_w^\alpha}{\delta_w^\alpha} (w^{\alpha*} - \langle w^\alpha \rangle^\alpha) \quad (6)$$

The interfacial terms for mechanical interactions between the solid and liquid phases are distinguished considering two regimes: the slurry regime in which solid grains are small and freely move in the liquid phase; and the porous regime in which they become larger, heavier and aggregate to fixed regions (e.g., packed beds of equiaxed grains or mold boundaries).

$$\text{slurry regime} \quad \mathbf{M}^{l,d} = -\mathbf{M}^{s,d} = \frac{1}{2V_e} \rho^l A_e C_D |\langle \mathbf{v}^s \rangle^s - \langle \mathbf{v}^l \rangle^l| (\langle \mathbf{v}^s \rangle^s - \langle \mathbf{v}^l \rangle^l) \quad (7)$$

$$\text{porous regime} \quad \mathbf{M}^{l,d} = -\mathbf{M}^{s,d} = -\frac{(g^l)^2 \mu^l}{K} \langle \mathbf{v}^l \rangle^l \quad (8)$$

where $\bar{\mathbf{v}}^{\alpha*}$, $\bar{w}^{\alpha*}$, $\bar{h}^{\alpha*}$ are respectively the averages of velocity, concentration and enthalpy of phase α over the interfacial area; S_V is the interfacial area concentration; D_w, D_T represent the solutal and thermal diffusivities; $\delta_w^\alpha, \delta_T^\alpha$ are the characteristic solutal and thermal diffusion lengths [13]; A_e, V_e are the cross section area and the volume of grains respectively; C_D is the drag coefficient [14]; the permeability K is modelled by the Kozeny-Carman equation.

The distribution of solid grains is modelled by the population balance equation as

$$\frac{\partial N}{\partial t} + \nabla \cdot (N \langle \mathbf{v}^s \rangle^s) = S_{nucl} \quad (9)$$

where N is the grain density per unit volume and S_{nucl} represents the nucleation source.

2.2. Resolution method and numerical implementation

Strong coupling exists between the quantities in the above equations, describing at the same time macroscopic transports and microscopic phenomena. It requires dedicated algorithms to find the solution of the set of non-linear equations. In this section, the implementation of a splitting method proposed earlier [1,2] is presented. The general resolution algorithm is shown in Figure 1. In the first step, the mixture energy conservation obtained by adding up equations (4), written for the solid and liquid phases with equal intrinsic average temperatures for the phases, i.e. equation (10) in Figure 1, is solved to determine the average specific enthalpy $\langle h \rangle$. Note that the phase densities are assumed constant and equal for all phases in the present model. In the next step, the evolution of the total mass, of the grain density and of the mass of species are computed in the transport stage. For that purpose, Eqs. (2), (3) and (9) are solved by keeping only the transport terms and neglecting those related to nucleation and growth of the equiaxed grains, which leads to Eqs. (11-13) in Figure 1. The values deduced from the transport stage for the solid fraction, g_{tr}^s , and the compositions $\langle w^s \rangle_{tr}^s$ and $\langle w^l \rangle_{tr}^l$, are used to initialize the subsequent nucleation and growth stage. The number of nucleated grains is determined by Eq. (14). The growth rate of solid grains, $\Gamma^s = -\Gamma^l$, and the composition at the interface, w^{s*} and w^{l*} , are determined by the energy balance and the interfacial solute mass balance, Eqs. (15) and (16) in Figure 1 respectively. Knowing these quantities it is possible to determine the variations of the solid fraction as well as those of the intrinsic average compositions for each phase by Eqs. (17) and (18) and hence the actual solid fraction, g_{gr}^s and compositions, $\langle w^s \rangle_{gr}^s$ and $\langle w^l \rangle_{gr}^l$. The final evolution of quantities includes contributions of these two stages. The solid and liquid velocities as well as the pressure are determined by solving the momentum conservation Eqs. (2) and the continuity Eq. (19). At each time-step, iterations are performed until all variables are converged, as schematized by the CV diamond and the feedback arrow on the left hand side of Figure 1. This ensures coherency between the solution of the complete set of equations with the FEM at the macroscopic scale (Eqs. (10-13), (19) and (2) in Figure 1) with the local solutions for the microscopic processes described by Eqs. (14-18) in Figure 1.

In the work presented here, a particular treatment is carried out by adding the artificial diffusion terms to Eqs. (11-13) in order to stabilize the FEM resolution of the purely advective transport equations. The artificial diffusion coefficient D_M used in this study depends on the characteristic mesh sizes, $he_{v\alpha}^2$, and on the spatial variation of velocities, as seen in Figure 1. This treatment is inspired by the treatments used for supersonic reacting flows [15] but it is modified to adapt to solidification modelling. In order to respect the mass conservation and to ensure consistence of all transported quantities, the same artificial coefficient is applied to the energy, Eq. (10). All terms related to the artificial diffusion are marked with yellow squares in Figure 1.

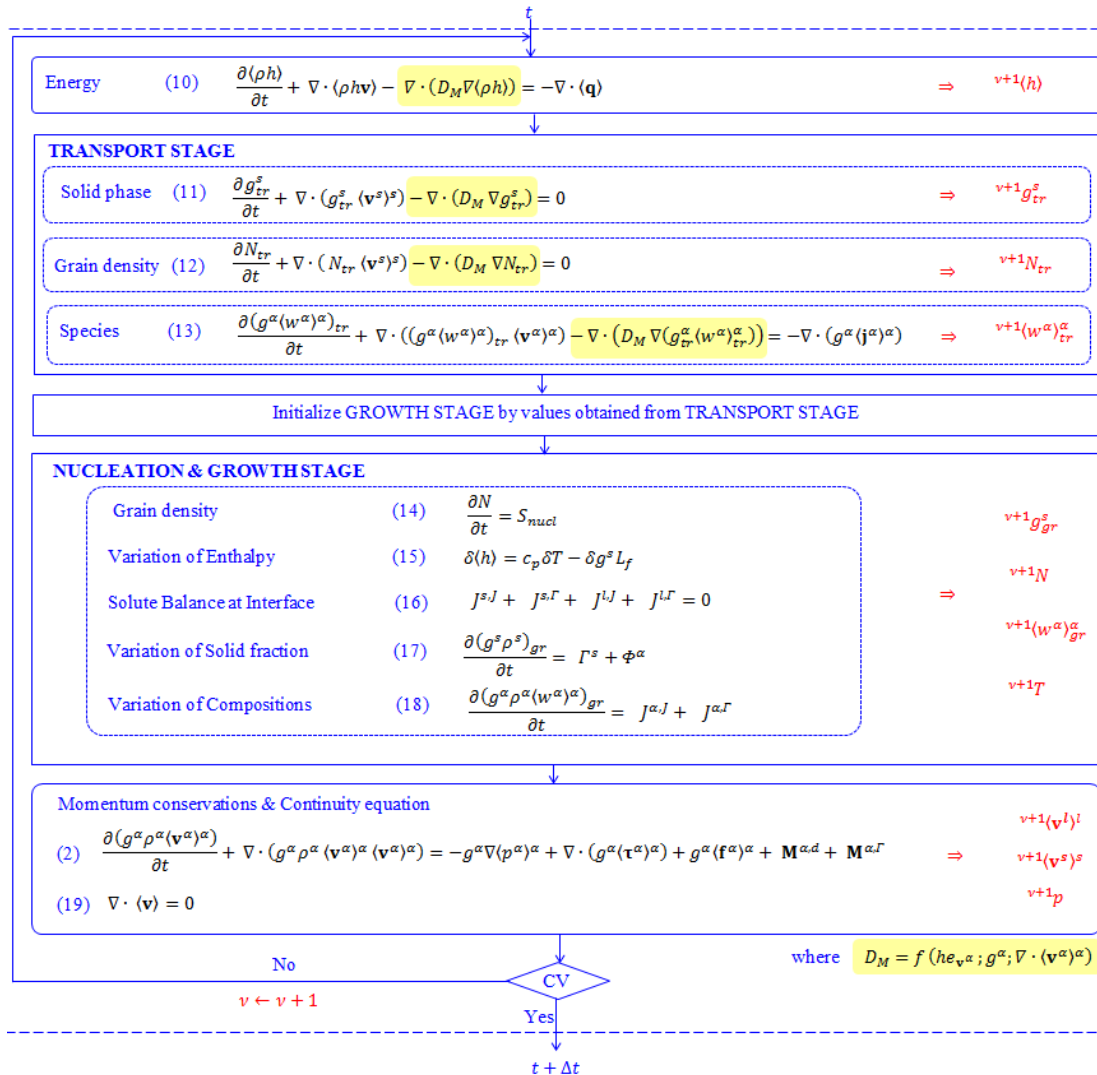


Figure 1. Resolution algorithm

3. Simulation results and discussion

3.1. 1D simulation – Study of the growth stage

For verification purposes the model is first tested for a case of pure diffusion. This tests its capacity to account for the grain growth kinetics at the microscopic scale. Both liquid convection and solid transport are neglected. Solidification occurs in a one-dimensional manner. This is achieved by defining a 1 mm thick and 100 mm wide domain cooled from one of its narrow sides. Six sensors are defined along the sample, two at both ends and four between them with a regular spacing of 2 cm. The thermophysical properties of the material are taken from reference [16] and are representative of a binary Al-4wt%Cu alloy, except for the solute diffusivity coefficients and the grain density. These two parameters are control parameters. They are used to switch between a case with a very high solute diffusion, so-called “infinite” diffusion and the other case for a lesser diffusion, so-called “finite” diffusion, as indicated in Figure 2.

Figure 2 shows a comparison of the cooling curves (left) and solid fraction evolutions (right) at six sensors between the “infinite” solute diffusion case (green curves) and the “finite” diffusion case (red curves): a) with high diffusion in the solid phase; b) with no solute diffusion in the solid phase. In the

case with “finite” diffusion, it can be noticed that the first red curve on the cold side presents a recalescence close to the liquidus temperature, which is not computed when liquid composition is well mixed, i.e. for the green curves. This phenomenon is captured by the present model because it takes into account nucleation and grain growth kinetics. It depends on both the values of the grain density and the liquid diffusion coefficient. Yet the red curves are found to depart very little from the green curves that were verified to exactly retrieve the lever rule approximation. With high values of the Lewis number (the ratio between heat diffusivity and mass diffusivity), solidification at microscopic scale is dominated by solute diffusion. A limited solute diffusion results in a slow phase transformation at the beginning of solidification which is illustrated by a discrepancy of solid fraction evolutions between the “infinite” and “finite” diffusion cases. The discrepancy decreases as solidification progresses. This can be explained by the fact that during solidification only a part of the liquid solute content is transferred to the solid due to solute partitioning. The rest that is rejected from the solid builds up in the liquid between grains. The increase of solutal gradients around the solidification front and the extension of solid-liquid surfaces accelerate solute mixing. In the case of no solute diffusion in the solid phase, a formation of eutectic structure is predicted toward the end of solidification when the eutectic temperature is reached, as shown in Figure 2b. The amount of eutectic is proportional to the final vertical jump of the solid fraction curves to reach unity. It was also checked that the green curves in Figure 2b tends toward the solution with the Gulliver-Scheil approximation, further validating the implementation of the microscopic growth stage.

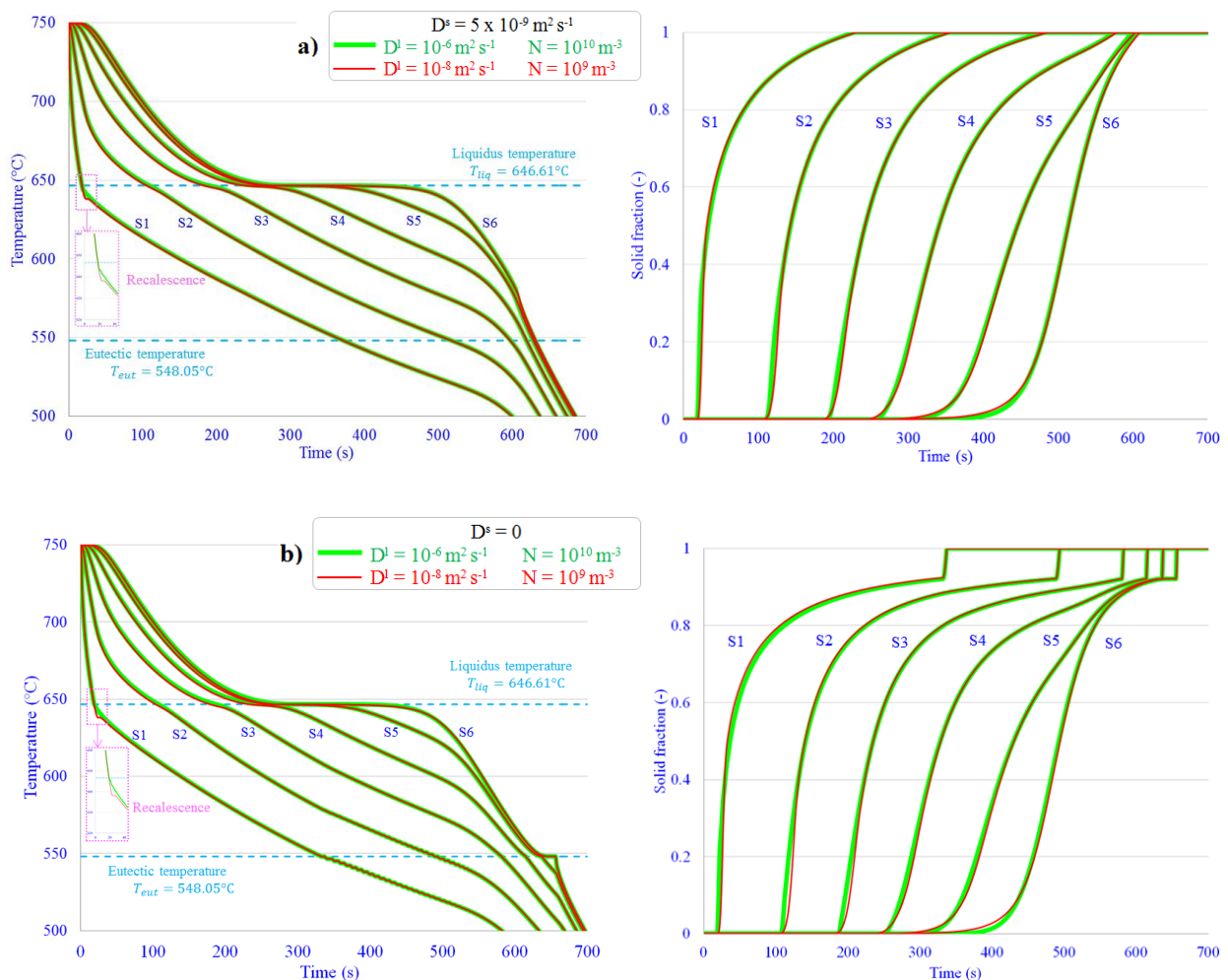


Figure 2. Cooling curves (left); Temporal evolutions of the solid fraction (right)

3.2. 1D simulation – Study of the transport stage

In the previous section, the growth stage combined with the energy resolution showed the ability of the present model to model solidification without motion. In the present section, the transport stage is carried out by studying the sedimentation of solid grains. This is first done neglecting the nucleation and growth stages, i.e. with a given number of grains of constant size. The properties chosen for this test come from a binary Sn-5wt%Pb [2]. At the beginning, the grains are distributed with a fixed density, 10^9 grains m^{-3} , within a subdomain of 20 mm to 80 mm of a 10 mm \times 100 mm sample, as shown in Figure 3a at time $t = 0$ s. The fraction of solid in this subdomain, shown in Figure 3c-top, is 0.1, thus fixing the grain radius to 288 μm . The intrinsic solute composition of the liquid is 5 wt%Pb in the entire sample and the intrinsic composition of the solid is 0.328 wt%Pb where the solid is present and zero elsewhere. The average composition is thus not homogeneous at 5 wt%Pb. The initial temperature, 498.057 K, is computed by using the lever rule so that it directly corresponds to the solid fraction and the compositions. An unstructured triangular mesh with a size of 0.5 mm and a constant time step 0.01 s are used.

The sedimentation process is illustrated through the maps of solid fraction and its profiles at 2 s, 5 s and 10 s, as shown in Figures 3a and 3c-top. From the initial state, the solid grains fall with a velocity of around 7 mm s^{-1} , computed through a balance of forces acting on the grains (Figure 3b). The first grains arrive at the sample bottom after 3 s and begin to accumulate until the characteristic packing fraction is reached (taken as 0.3). During the computation, the velocity of the grains moving towards the zone near the packing area is adjusted so that these grains can land smoothly in the packed bed, i.e. reaching $\langle \mathbf{v}^s \rangle^s = 0$ at the packing limit. To be more specific, on the one hand, the solid velocity is reduced by viscous effect, as the viscosity strongly increases when the solid fraction is close to the packing value [17]. On the other hand, if the grains go so fast, their velocity is multiplied by a factor calculated by dividing their current distance to the packing limit by the distance which they can go due to their velocity projected on the gradient of solid fraction. Without these numerical remedies, the solid fraction of the packed zone can exceed the packing fraction, which is caused by a brutal stop of grains arriving in the packed area.

As the grain motion involves the transport of other quantities, it is important to verify the consistency of their transports. Figure 3c-center presents the profiles of the average composition at 0 s, 2 s (before the grains have reached the bottom of the domain), 5 s (accumulation below the packing limit) and 10 s (end of packing). They show consistency with those of the solid fraction. When the solid grains sediment, solute-rich liquid with 5wt%Pb rises and fills the region left by the grains. The average composition of 3.6 wt% Pb in the negative segregation zone at the bottom corresponds precisely to the final state of 30% of solid at 0.328 wt%Pb and 70% of liquid at 5 wt% Pb. In addition, as expected for a pure transport simulation, the temperature does not change during this process. This is seen in Figure 3c-bottom. A good overall conservation of all quantities is also verified, the maximum relative errors of solute mass and energy being about 10^{-6} and 10^{-5} , respectively.

This section deals with difficulties in FEM modelling of purely advective transport, as its solution presents numerical instabilities. To remedy these difficulties an addition of adequate artificial diffusion is necessary along with the aforementioned modifications of the solid-velocity calculation.

These remedies are necessary to be able to solve the equations of the present model with the FEM. In this work the addition of artificial diffusion was done and examined very carefully, in order to ensure consistency between all the quantities and the conservation of mass and energy.

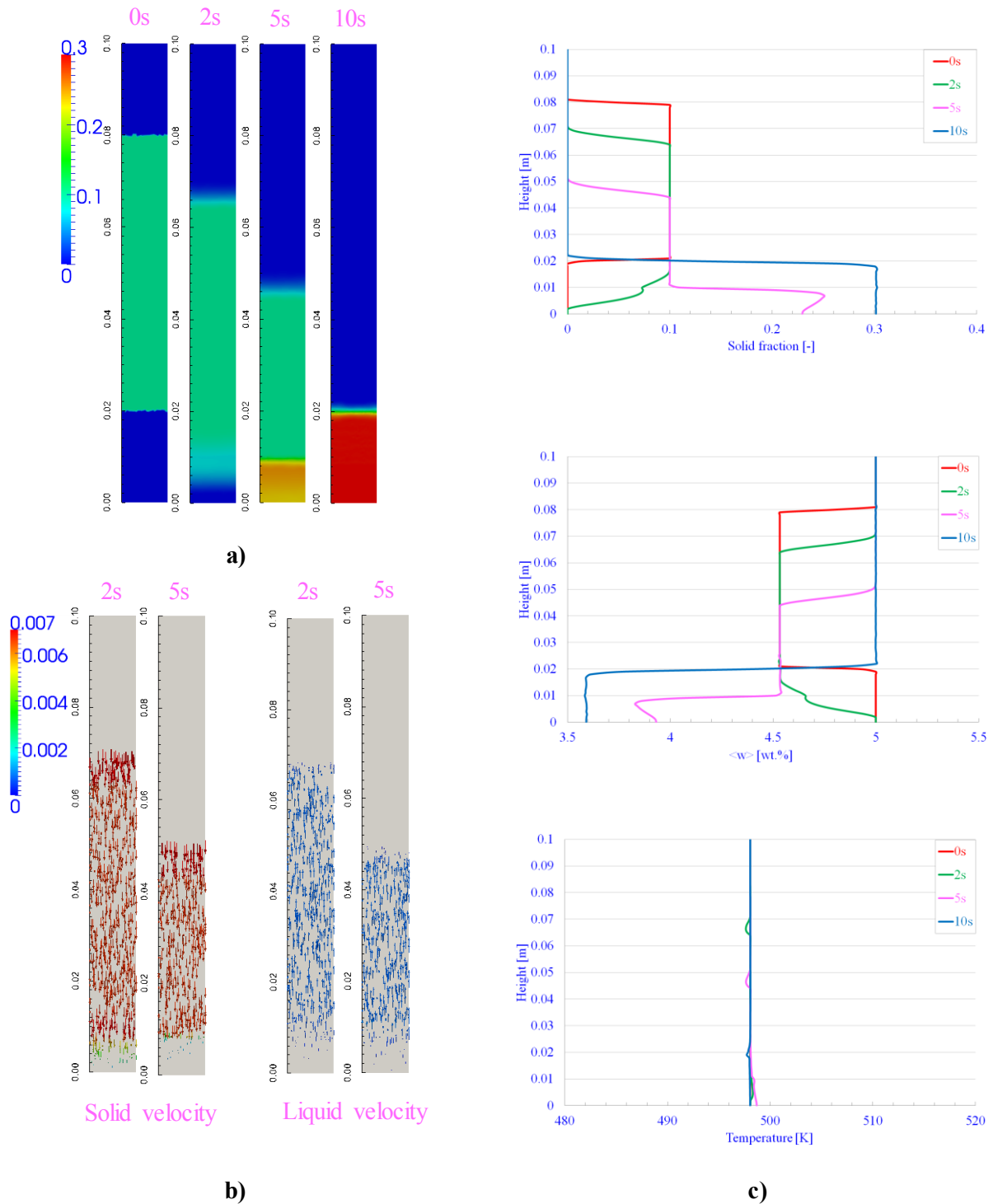


Figure 3. a) Solid fraction distribution at 0 s, 2 s, 5 s and 10 s.
 b) Vectors of the solid phase (left) and of the liquid phase (right) at 2 s and 5 s.
 c) Profiles of the solid fraction (top), the average composition (center) and the temperature (bottom) at 0 s, 2 s, 5 s and 10 s.

3.3. 2D solidification simulations

Following the 1D simulations, two 2D solidification cases are simulated and compared. Both cases involve a Sn-5wt%Pb alloy. Case 1 accounts for thermo-solutal liquid convection but considers a fixed solid phase and Case 2 includes both liquid convection and solid movement due to liquid advection and sedimentation. The sample of 0.06 m x 0.1 m size is cooled from the left hand side. The initial liquid metal temperature is 260°C. An unstructured triangular mesh with constant size, 1 mm, and a time step of 0.01 s are used.

In Case 1 there is no solid transport, therefore the terms relating to the solid motion in the equations presented in section 2 are set equal to zero; the packing fraction is considered as equal to zero. In Case 2, the full model is applied accounting for grain growth and transport phenomena, in which the solid phase is supposed to be stationary when its fraction reaches the packing value.

The simulation results of Case 1 and Case 2 are compared in Figures 4 and 5. Figure 4 displays the solid velocity vectors, the liquid velocity streamlines and the solid fraction distribution. The black line represents the limit between the packed and the slurry zones. The solidification sequence in these two cases is quite different. In Case 1, initial solid grains nucleated on the cooled side are fixed there and when solidification proceeds, newly formed solid grains attach to the existing solid layers. The global solidification front thus advances from left to right. This is close to a columnar growth situation. In Case 2, after nucleation due to the gravity force and the liquid advection, solid grains sink downwards to the bottom as well as are transported far away by liquid flow. During this process, some grains travel in the slurry region and strongly affect the movement of the liquid phase, while the largest grains settle and accumulate as an increasing solid layer forming from at the bottom.

In addition, solidification progresses faster in Case 2 compared to Case 1. This can be explained by the fact that the solid grains that settle in the vicinity of the cold mold are replaced by a hotter liquid phase. Consequently, the global heat exchange between the metal and the mold takes place more efficiently and results in faster solidification, as shown at 360 s.

The final macrosegregation maps are shown in Figure 5. Although higher solute content is found at the bottom area for both cases, its formation mechanism is quite different. In Case 1, it is primarily governed by natural convection in the zone with relatively high liquid fraction. The solid zone extends from left to right and the rejected solute is progressively accumulated in the bottom-right region due to the higher density of the solute-enriched liquid. A high solute concentration is therefore found at the bottom-right corner.

For Case 2, at the initial stage, sedimentation of solute-depleted grains leads to a rigid solid layer and a negative segregation in the lower part. As the process evolves, an intergranular downward flow builds up in the packed porous zone, which brings the solute from the upper to the lower region. At the very bottom of the cavity, the intensity of the flow through the mushy zone is sufficient to lead to remelting and finally forms a positive segregation.

Through this section, we study the effect of the solid transport on the solidification sequence as well as the formation of macrosegregation. The results of the solid fixed case obtained from the present formulation with high values of solute diffusion coefficients retrieve those simulated with the lever rule model from the literature using FVM [2], and our FEM simulation. For the solid transport modeling, further evaluation that would be necessary will be carried out in the future.

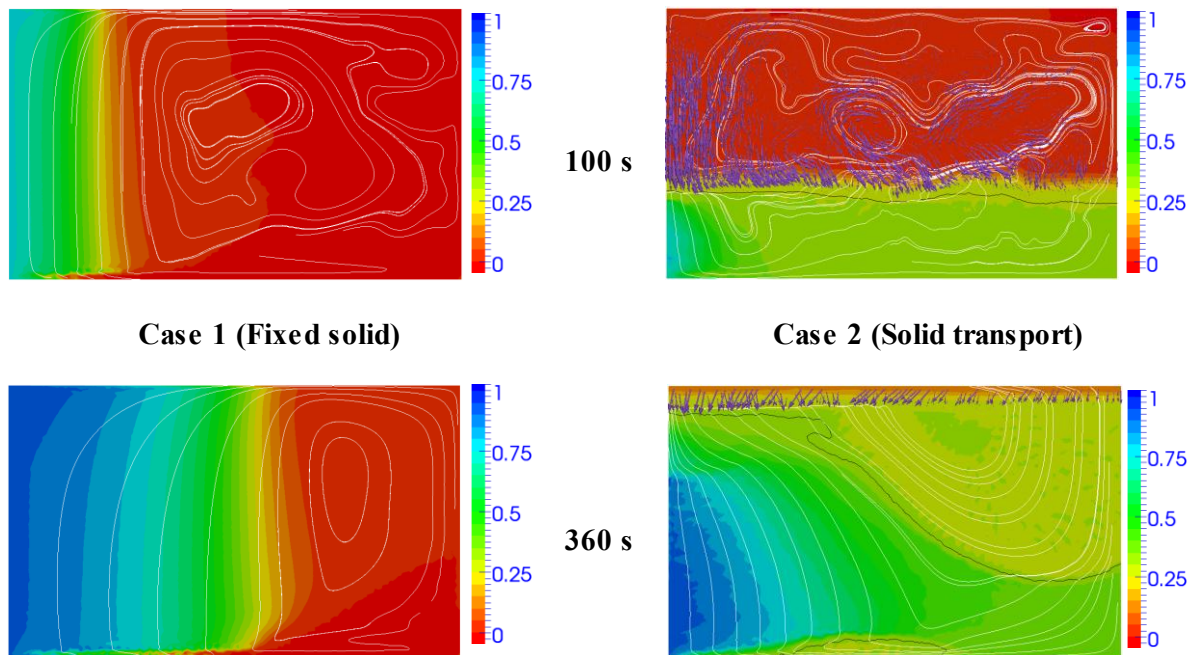


Figure 4. Solid fraction distribution displayed with (violet arrows) solid velocity vectors and (white contours) liquid velocity streamlines.

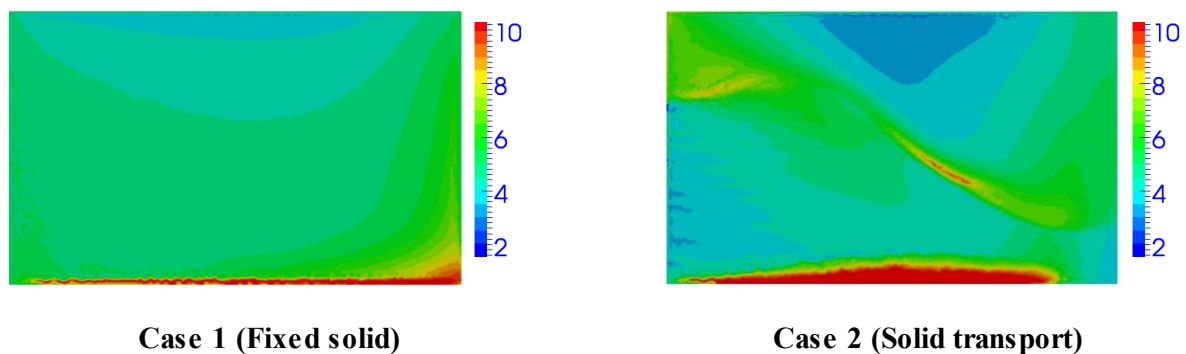


Figure 5. Final macrosegregation maps.

4. Conclusion

This paper presents a FE numerical model taking into account microscopic processes as well as the macroscopic transport phenomena. The resolution is based on splitting scheme, in which the transport stage is solved independently from the nucleation and growth stages. The coupling between the two stages is achieved through an iterative procedure. Simulations were first carried out to test the capabilities of this model to deal with pure growth and pure transport situations. Then the model is applied to solidification with a fixed solid phase and with the transport of solid grains. The main results can be summarized as follows.

- The present model incorporates a macrosegregation approach able to simulate solidification paths with finite diffusion in solid and liquid phases, including the recalescence phenomenon.

- The vertical sedimentation of particles has been simulated by the FE model and consistent time and space evolutions of all quantities during transport have been verified.
- Compared to the fixed solid case, results obtained with this new FE model for solid transport show an important influence of solid motion on solidification progression and on formation of macrosegregation.

Simulation results would be further assessed by comparing with other works and experimental results. Combined with mesh adaptation techniques, the present model should provide industry with a promising tool for modeling castings. Further development should encompass the extension to multicomponent alloys and the consideration of various morphologies of the solid phase.

Acknowledgments

The financial support from ArcelorMittal, Industeel, Aubert & Duval, Ascometal and Aperam is gratefully acknowledged.

References

- [1] Založnik M and Combeau H 2010 *Comput. Mater. Sci.* **48** 1-10
- [2] Založnik M, Kumar A and Combeau H 2010 *Comput. Mater. Sci.* **48** 11-21
- [3] Ni J and Beckermann C 1991 *Metall. Trans. B.* **22** 1991-349
- [4] Beckermann C and Viskanta R 1993 *Appl. Mech. Rev.* **46** 1-27
- [5] Wang C Y and Beckermann C 1996 *Metall. Mater. Trans. A.* **27** 2754-64
- [6] Wang C Y and Beckermann C 1996 *Metall. Mater. Trans. A.* **27** 2765-83
- [7] Ludwig A and Wu M 2002 *Metall. Mater. Trans. A* **33** 3673-83
- [8] Wu M, Ludwig A, Buhrig-Polaczek A, Fehlbier M and Sahm P R 2003 *Int. J. Heat. Mass. Tran.* **46** 2819-32
- [9] Wu M, Li J, Ludwig A and Kharicha A 2013 *Comput. Mater. Sci.* **79** 830-40
- [10] Wu M, Li J, Ludwig A and Kharicha A 2014 *Comput. Mater. Sci.* **79** 267-85
- [11] Combeau H, Založnik M, Hans S and Richy P E 2009 *Metall. Mater. Trans. B.* **40** 289-304
- [12] Rappaz M, Bellet M and Deville M 2003 *Numerical Modeling in Materials Science and Engineering* (Verlag Berlin Heidelberg New York : Springer)
- [13] Bedel M 2014 *Etude de la formation des structures de solidification et des macroségrégations en coulée semi-continue d'aluminium* chapter 2 p 55-66
- [14] Guillemot G, Gandin Ch A and Combeau H 2006 *ISIJ Int.* **46** 880-95
- [15] Cook A W and Cabot W H 2004 *J. Comput. Phys.* **195** 594-601
- [16] Ni J and Beckermann C 1993 *J. Mater. Process. Manuf. Sci.* **2** 217-231
- [17] Graham A L 1981 *Appl. Sci. Res.* **37** 275-86